Review article

Microstructure and mechanical behavior of Ti–6Al–4V produced by rapid-layer manufacturing, for biomedical applications

L.E. Murr[a,*], S.A. Quinones[b], S.M. Gaytan[a], M.I. Lopez[a], A. Rodela[a], E.Y. Martinez[a], D.H. Hernandez[a], E. Martinez[a], F. Medina[c], R.B. Wicker[c]

[a] Department of Metallurgical and Materials Engineering, University of Texas at El Paso, El Paso, TX 79968, USA
[b] Department of Electrical and Computer Engineering, University of Texas at El Paso, El Paso, TX 79968, USA
[c] Department of Mechanical Engineering and Keck Center for 3D Innovation, University of Texas at El Paso, El Paso, TX 79968, USA

ARTICLE INFO

ABSTRACT

The microstructure and mechanical behavior of simple product geometries produced by layered manufacturing using the electron beam melting (EBM) process and the selective laser melting (SLM) process are compared with those characteristic of conventional wrought and cast products of Ti–6Al–4V. Microstructures are characterized utilizing optical metallography (OM), scanning electron microscopy (SEM) and transmission electron microscopy (TEM), and included α (hcp), β (bcc) and α' (hcp) martensite phase regimes which give rise to hardness variations ranging from HRC 37 to 57 and tensile strengths ranging from 0.9 to 1.45 GPa. The advantages and disadvantages of layered manufacturing utilizing initial powders in custom building of biomedical components by EBM and SLM in contrast to conventional manufacturing from Ti–6Al–4V wrought bar stock are discussed.

© 2008 Elsevier Ltd. All rights reserved.

Contents

* *Corresponding address:* Department of Metallurgical and Materials Engineering, University of Texas at El Paso, 500 W. University Ave.ESC Room M-201, El Paso, TX 79968, USA. Tel.: +1 915 747 6929; fax: +1 915 747 8036.
E-mail address: lemurr@utep.edu (L.E. Murr).

1.   Introduction

Metal orthopedic joint replacements (hip or knee joints) and bone plate surgeries now number in the millions worldwide annually, with knee joint replacement surgeries in the US alone numbering in excess of 300,000 annually. Most hip and knee implants are fabricated from wrought or cast bar stock by CNC, CAD-driven machining, or powder metallurgy (PM) production methodologies; including HIP and powder injection molding of near-net-shape components (Long and Rack, 1998; Gibson, 2005). Most of these millions of joint replacements, bone plates, etc. are generic, mass-produced components which do not work well with patients having an abnormal or unusual anatomy. In these situations, custom-designed implant components are preferred or required. This is also particularly true for cranioplasty especially where the missing piece of bone is large, requiring an implant component to be fabricated to follow the overall skull curvature (Eufinger and Saylor, 2001). A further challenge in implant component fabrication is the necessity to manufacture complex shapes, including thin-walled sections, where cutting operations can take a long time owing to significant material removal; up to 80% of bar stock from which knee implants are fabricated is converted to metal chips or scrap material.

In recent years solid freeform fabrication (SFE) — also variously called rapid prototyping (RP), layered manufacturing (LM) or rapid manufacturing (RM) — or direct digital manufacturing (DDM) has provided a "renaissance in manufacturing" (Chuna et al., 2003). SFF technologies are able to fabricate complex shapes of a custom-designed component using precursor powders to build these shapes through computer-controlled, self-assembly by sintering or melting powder layers using either a laser or an electron beam. Until recently, SFF technologies were not able to build custom-designed components from biocompatible metal or alloy powders such as stainless steel, Ti, Ti–6Al–4V and other Ti-alloys, and cobalt–chromium (Co–Cr) alloys (29% Cr, 6% Mo, balance Co by weight). Furthermore, desirable monodispersed metal or alloy powders with a uniform rapid solidification microstructure were also not generally available until early in this century.

Cormier et al. (2004) recently described the characterization of H13 steel (components using electron beam melting (EBM), while Harrysson and Cormier (2005) described the EBM fabrication of custom orthopedic implants from commercially available powders of H13 steel and Ti–6Al–4V. However neither the powders nor the resulting EBM fabricated components were characterized in the context of their microstructures or associated mechanical behavior. More recently, Hiemenz (2007) discussed the EBM process generally while Murr et al. (in press) have compared the microstructure and mechanical behavior of both the precursor Ti–6Al–4V powder and simple EBM fabricated components along with the microstructure and mechanical properties of several commercial, wrought products of Ti–6Al–4V. In addition to these papers describing EMB-DDM utilizing metal powders to fabricate biomedical and related components, Vandenbroucke and Kruth (2007) have also recently described selective laser melting of biocompatible metals and alloys for RM.

Niinomi (2008) has intimated in a recent review article that, "Among metallic biomaterials such as stainless steels and Co–Cr alloys, Ti and its alloys exhibit the most suitable characteristics for biomedical applications because of their high biocompatibility, specific strength, and corrosion resistance (Niinomi, 2001)". Indeed, the majority of hip and knee implants over the past decade have been variously processed Ti–6Al–4V (Long and Rack, 1998; Chuna et al., 2003; Niinomi, 2007; Yaszemski, 2004) and recent EBM-RM produced implants and other experimental products fabricated from commercial Ti–6Al–4V powders have shown exceptional promise for custom-designed implant components (Harrysson and Cormier, 2005; Christensen et al., 2007; Christensen, 2007; Murr et al., in press).

In this paper we review the thermomechanical processing of wrought and cast Ti–6Al–4V products along with their associated microstructure and mechanical behavior. Microstructures are characterized by optical and electron microscopy (including scanning electron microscopy (SEM) and transmission electron microcopy (TEM) and include α(hcp : a = 0.295 nm: c = 0.466 nm) and β(bcc : a = 0.33 nm) phase morphologies, dislocation substructures, twinning, martensitic transformations, and other phases (Destefani, 1990; Lampman, 1990; Eylon and Froes, 1990; Niinomi, 1998; Ding et al., 2002; Froes, 2004; Leutjering and Williams, 2003; Williams and Leutjering, 1980; Williams et al., 1987). These phase morphologies as well as dislocation, twin, and martensitic substructures affect mechanical behavior — in particular indentation hardness and tensile properties. Additionally and more importantly, we discuss and compare Ti–6Al–4V products fabricated from precursor powders utilizing EBM and laser melting (specifically selective laser melting (SLM)); especially comparing their microstructure and mechanical behavior. Finally, we discuss the advantages and disadvantages of EBM and laser melting-rapid prototype manufacturing especially in the context of prospects for Ti–6Al–4V custom implant production and the tailoring of biomedical component properties and performance through systematic microstructure-mechanical behavior control during powder layer manufacturing.

2.   Wrought and cast Ti–6Al–4V: Thermomechanical processing, microstructure, and mechanical behavior

Manufacturing processes associated with Ti products include (1) casting (2) wrought (forging/milling from ingots), (3) powder metallurgy (P/M), and relatively new processing methods by direct digital manufacturing such as electron beam melting (EBM), direct metal laser sintering (DMLS), laser-engineered net-shaping (LENS) and ultrasonic consolidation (UC). Wrought products account for 70% of the Ti and Ti alloy market (Lampman, 1990). Wrought Ti materials undergo several melt cycles in order to remove impurities such as hydrogen and other volatiles in order to produce a high purity ingot that is forged or milled into the final product (Lampman, 1990). Critical factors associated with processing wrought Ti alloys include (1) alloying, (2) the melting process used in ingot processing, (3) mechanical working history, (4) heat treatment temperatures and cooling rates and (5) aging treatment.

For Ti alloys, cast parts can be produced with properties similar to or superior to wrought products, with enhanced

crack propagation and creep resistance properties. Post-treatment of cast products include heat treatment and/or hot isostatic pressing (HIP) to eliminate porosity introduced during the casting process (Destefani, 1990). The microstructure of cast Ti–6Al–4V consists of an $\alpha + \beta$ platelet structure that is transformed from a dendritic β structure during solid state cooling, resulting in a microstructure that is comparable to the β processed wrought structure with corresponding properties. This in effect prevents the dendritic structure from solidifying upon cooling and can be attributed to the $\beta \rightarrow \alpha + \beta$ transformation associated with $\alpha + \beta$ alloys at 995 °C (Eylon and Froes, 1990).

The advantage of wrought products vs. cast products is that the former can be thermomechanically treated (cold/hot working plus heat treatment) into a final shape, thus enabling tailoring of desired mechanical properties. Net shape products associated with casting and powder metallurgy (P/M) are fabricated in the final shape, which limits further processing to heat treatments such as solution treatments or temporary annealing with hydrogen. While hydrogen treatment results in superior properties, the effect of this treatment is dependent on size and may not have the desired effect on larger components due to the associated lower quench rates (Eylon and Froes, 1990). Like cast products, the goal of processing by powder metallurgy is to reduce or eliminate the cost of machining. The microstructure of P/M products depends on the initial powder, compaction and post thermal processing treatments. Density is critical for Ti alloys, since porosity has detrimental effects on fatigue and fracture properties, and fully dense parts are critical (>99% dense) (Eylon and Froes, 1990). For this reason, the range of build parameters should be tested for this alloy in order to determine the full range of mechanical properties that can be tailored through this technique.

At room temperature, the microstructure of pure Ti consists of 100% alpha. For $\alpha + \beta$ alloys, when α and β stabilizers (such as aluminum and vanadium) are added as alloy constituents, the beta phase begins to appear at grain boundaries (Lampman, 1990). Other alloying elements can be added, and each alters the $\alpha \rightarrow \beta$ transition temperature. When α stabilizers are added (e.g. aluminum), the $\alpha \rightarrow \beta$ transition temperature is increased, and when β stabilizers are added (e.g. vanadium), the $\alpha \rightarrow \beta$ transition temperature is decreased. For instance, for pure Ti, the transition temperature is 885 °C, and for the Ti–6Al–4V alloy the transition temperature increases to 995 °C. In the case of the Ti–6Al–4V alloy, thermomechanical processing also has an effect on the amount of β phase in the final microstructure, where the percent β phase increases with increasing process temperature in the $\alpha + \beta$ phase, with 100% β formation when processed in the β phase, with or without deformation (Ding et al., 2002). Deformation of the β phase can create martensite (α'; hcp : a).

The α phase is observed in Ti–6Al–4V as equiaxed or acicular, and acicular morphology is present in $\alpha + \beta$ alloys that have been processed above the β phase (Lampman, 1990). The geometry of the α platelets will depend on the amount of deformation and cooling rate from the β phase, and decrease in width with increase in cooling rate (Lampman, 1990; Ding et al., 2002). With extensive deformation, the α platelets breakup into a spheroidized structure. Thus, there exists the
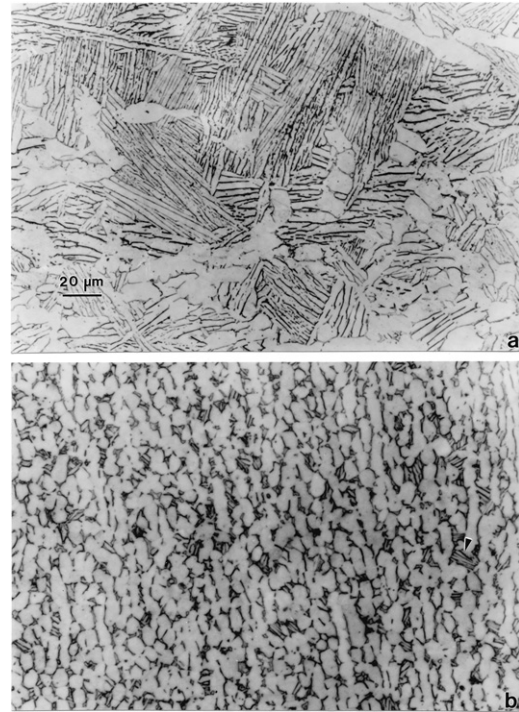

Fig. 1 – Optical metallographic views of two commercial, wrought Ti–6Al–4V alloys. (a) Coarse, plate-like (acicular) α with some intergranular β characteristic of a billet forged above the beta transus. (b) Equiaxed α and β (α/β) phase mixture for forged and solution treated billet. (From Murr et al. (in press)). Magnifications are the same as shown in (a).

possibility of producing Ti–6Al–4V components with a variety of microstructures and associated properties by varying the mechanical and thermal processing, and possibly the part dimensions, since larger components exhibit slower cooling rates (Lampman, 1990; Eylon et al., 1990).

Fig. 1 (Murr et al., in press) illustrates two extremes for wrought Ti–6Al–4V. Fig. 1(a) shows a predominantly coarse acicular (plate-like) α phase microstructure with very small amounts of β in the α phase boundaries. This microstructure represents a Ti–6Al–4V billet forged at 640 °C above the beta transus. Fig. 1(b) shows a mixed α/β equiaxed phase structure for a billet forged and solution treated 1 h at 950 °C, air-cooled; and then annealed 2 h at 700 °C.

Fig. 2 compares the ultimate tensile strength (UTS), 0.2% offset yield stress (YS(0.2%)) and elongation for the two wrought products in Fig. 1 with cast Ti–6Al–4V in the as-HIPed condition, and in the refined condition through the hydrogenation and dehydrogenation process for Ti alloys, also referred to as thermochemical processing (Sakaguchi, 2004; Akahori, 2000). Fig. 2 illustrates that although TCP can improve the UTS and yield stress (YS (0.2%)) for cast Ti–6Al–4V products, wrought materials generally exhibit superior mechanical behavior as processed, including elongation; which is reduced through TCP of the cast alloy (Fig. 2) (Niinomi, 1995).

Fig. 3 illustrates a transmission electron microscope (TEM) view of a section from the wrought Ti–6Al–4V in Fig. 1(a) showing the α and β substructure which characterizes the mechanical behavior illustrated in Fig. 2. Correspondingly,
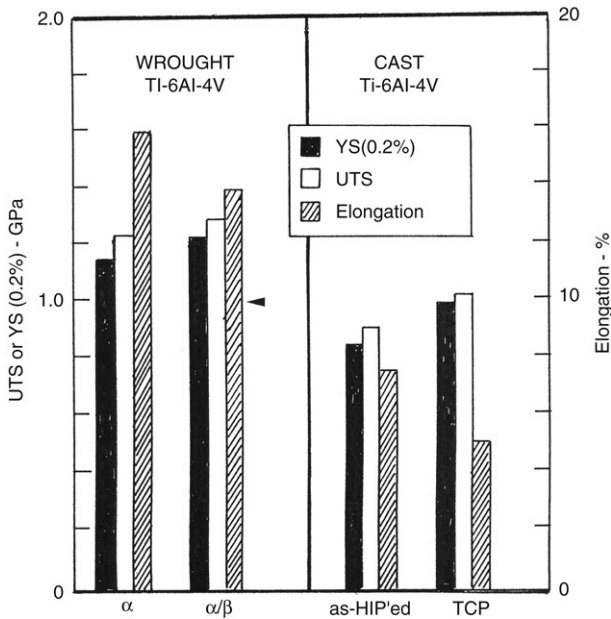
Fig. 2 – Ultimate tensile strength (UTS), 0.2% engineering offset yield stress (YS), and elongation of the α (Fig. 1(a)) and α/β (Fig. 1(b)) wrought Ti–6Al–4V compared with as-HIP'ed cast and cast TCP treated Ti–6Al–4V (cast data (left) from Niinomi (2008)).
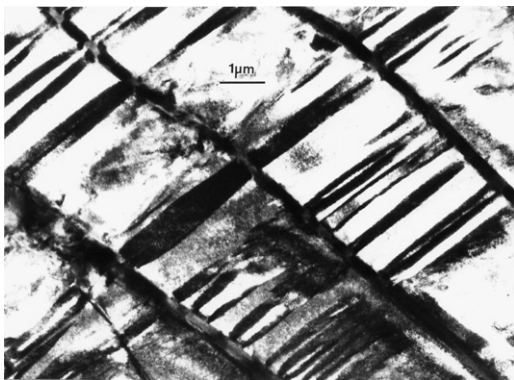
Fig. 3 – TEM (bright-field) image showing wrought Ti–6Al–4V acicular α-phase microstructure corresponding to Fig. 1(a).

Fig. 4(a) shows a dislocation network lying in a basal (0001) hcp α phase representing a dislocation density of $\sim$4 $\times$ 10^9 cm^{-2} (Murr, 1991) while Fig. 4(b) shows dislocations having a density in α phase regions of $\sim$$10^{10}$ cm^{-2} and corresponding to a region represented typically at the arrow in Fig. 1(b). Both Fig. 4(a) and (b) are TEM bright-field images representative of the microstructure in the wrought Ti–6Al–4V sample in Fig. 1(b). Fig. 5 shows a bright-field, dark-field (Murr, 1991) TEM image sequence for twins in the α phase in Fig. 1(b). While the various microstructures in Figs. 3–5, particularly deformation microstructures in Figs. 4 and 5 contribute to the mechanical behavior of wrought Ti–6Al–4V as shown in Fig. 2, the dislocation density is often the more prominent microstructural contributor to the strength and hardness. Murr
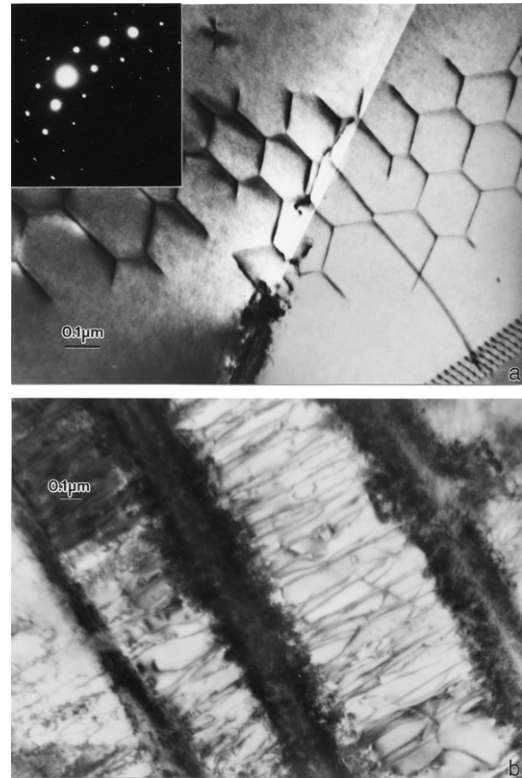

Fig. 4 – TEM (bright-field) images showing variations in dislocation substructures in α-phase regions of wrought Ti–6Al–4V characteristic of Fig. 1(a). (a) Hexagonal dislocation network structure in tilted (0001) phase orientation. (b) Heavy dislocation substructure within α phase regions.

(1991) have shown that for deformed copper, dislocations or dislocation density account for approximately 90% of the residual hardness or hardness change in contrast to grain size changes. The corresponding hardnesses corresponding to the wrought $\alpha + \beta$ Ti–6Al–4V in Fig. 1(a) and (b), respectively were HV 3.8 and 4.3 GPa; HRC 48 and 52, respectively. Most commercial, wrought Ti–6Al–4V products have HRC (Rockwell C-scale hardness) of 38 and a corresponding UTS and elongation of $\sim$1 GPa and 14%, respectively. However, Lampman (1990) has shown that when heat treatment is applied in the upper $\alpha + \beta$ phase field (955 °C) followed by water quench and aging, the UTS can be raised to 1.18 GPa and the elongation can extend to 16.5% (as shown in Fig. 2). Similar processing in the β phase field followed by water quench results in an α' (martensite) and β matrix, with prior β grain boundaries. This produces a UTS of 1.17 GPa with a corresponding elongation of only 8.5%. In both cases aging was performed at 540 °C for 4 h followed by air cooling (Lampman, 1990).

3.   Direct digital manufacturing by electron beam melting (EBM): Microstructures and mechanical behavior of Ti–6Al–4V components
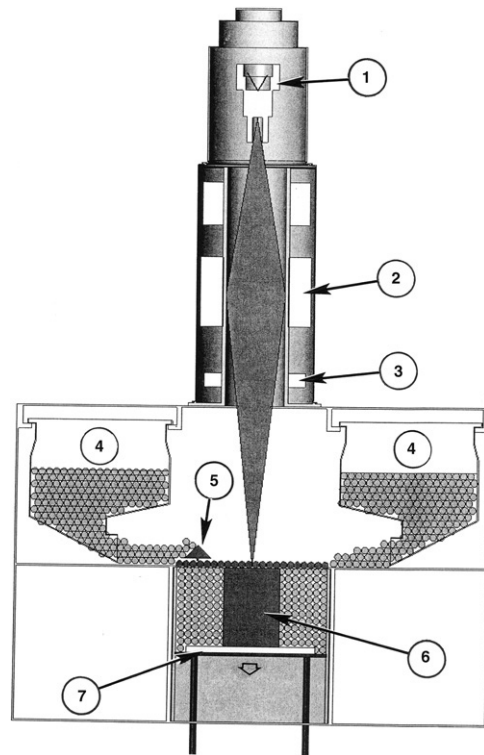
Fig. 6 illustrates a schematic view of the ARCAM EBM S400 system. The system builds layers approximately 100 µm thick
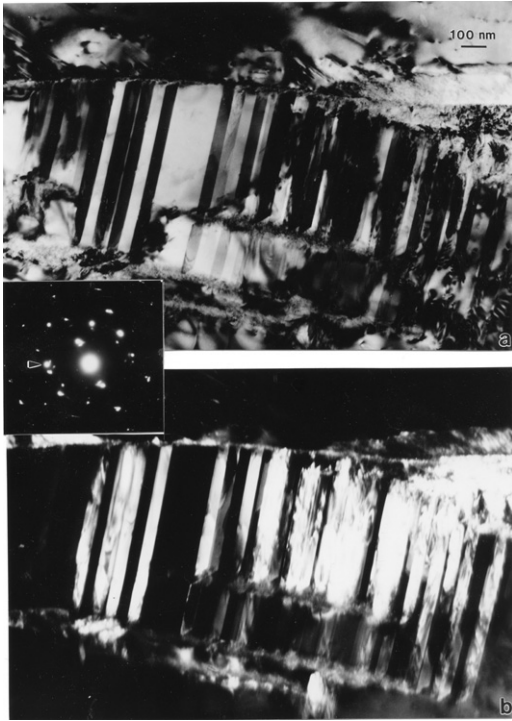
Fig. 5 – TEM bright-field (a) and dark-field (b) images of twins in $\alpha\prime$ martensite grain from the wrought α/β sample shown in Fig. 1(b). The selected-area electron diffraction (SAED) pattern insert shows the corresponding twin reflection (arrow) utilized for the aperture dark-field image.

Fig. 6 – EBM system schematic showing key components. The following numbers correspond to those circled in the figure: (1) Electron gun assembly; (2) EB focusing lens; (3) EB deflection coils (x-y); (4) Powder cassettes; (5) Powder layer rake; (6) cylindrical build test specimen; (7) Build table (From Murr et al. (in press)).

from atomized powder as represented in Fig. 7 for Grade 5 Ti–6Al–4V powder. The EBM system in Fig. 6 builds parts from the bottom up by scanning the focused electron beam ((2) and (3) numbered circles) at nominally 10^3 mm/s to selectively melt specific areas of the powder bed using a 3D-CAD system while powder is continuously added from the powder cassettes (4) to the top of the building part (Fig. 6(6)) in a vacuum. The powder rake shown at (5) in Fig. 6 moves laterally between the two cassettes (4) to evenly distribute the powder layers over the surface after each build layer is complete. The EBM system in Fig. 6 is an electron optical system essentially identical to a scanning electron microscope (SEM) (Murr, 1991) or an EB melting system where an electron gun ((1) in Fig. 6) generates a focused EB (2) in a vacuum which can be systematically scanned by deflection coils (3) across the building part (6) directed by a CAD design system. The electron gun (1) operates nominally at 60 kV to develop an energy density in the focused beam in excess of 10^2 kW/cm^2. Variations in beam current and scan rate as well as heating schedules involving the build table (7) and the building part (6) can allow for microstructure – property variations in the final product.

Fig. 8(a) and (b) illustrate some examples of biomedical components fabricated using the ARCAM system shown schematically in Fig. 6. While it can be observed that a finish by machining is required to achieve Fig. 8(b) from (a), it is apparent that near shape products can be achieved with significant machining reduction. A conventionally fabricated total knee (femoral and tibial) replacement is illustrated in
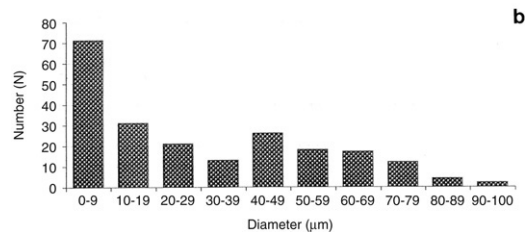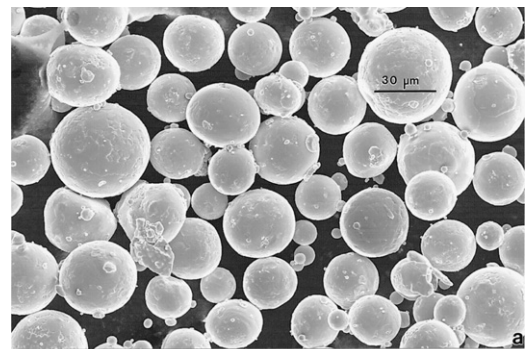
Fig. 7 – EBM system starting Ti–6Al–4V (Grade 5) powder features. (a) Field emission SEM image showing powder morphologies and sizes. (b) Histogram showing powder size distribution. Grade 5 nominal composition: 6% Al, 4% V, <0.2% Fe, <0.25% C, <0.2% O; balance Ti (in wt.%).
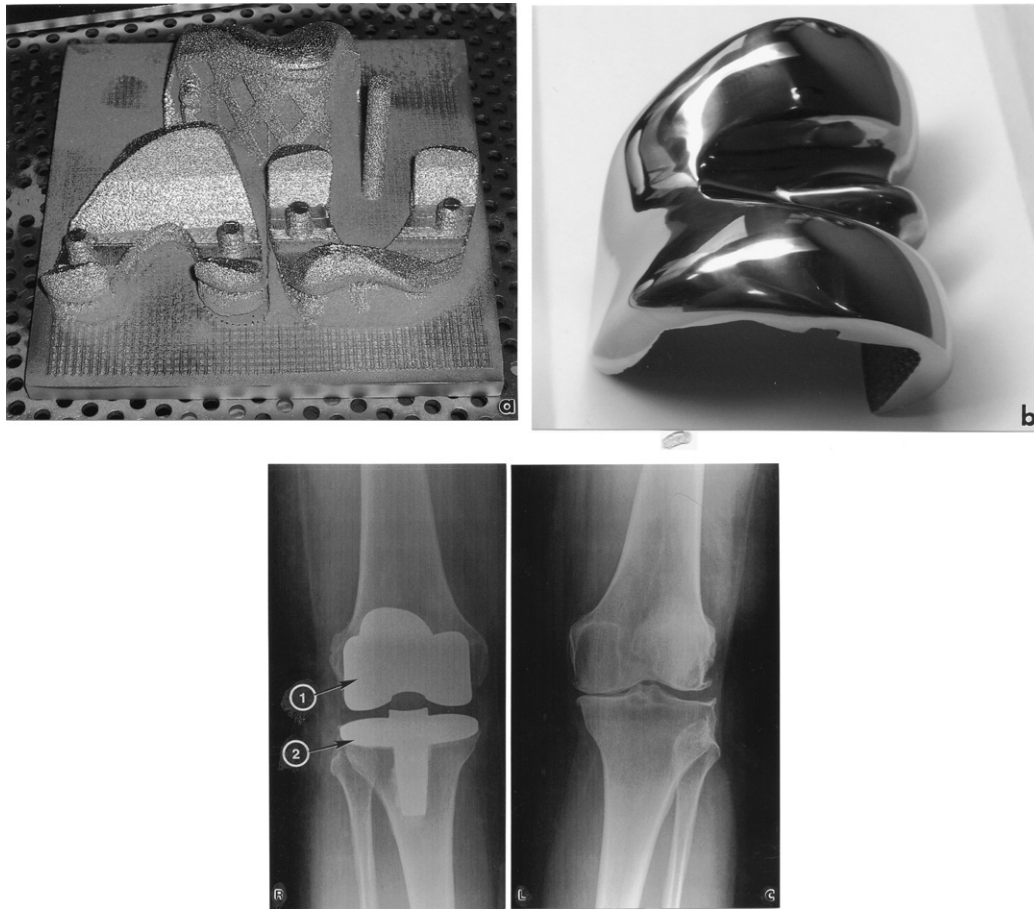
Fig. 8 – Examples of experimental biomedical replacements produced by EBM layer manufacturing. (a) As manufactured femoral components. (b) Finished component. Courtesy of Wayne Meyers, Stratasys, Inc. (c) Shows a wrought, manufactured total knee replacement implant in a right knee (R) of a female compared with the normal left (L) knee (front view X-ray). (1) Femoral component. (2) Tibial component with polyethylene top (not visible). (Courtesy of Dr. David Mansfield, Orthopaedic Surgery Group, El Paso, TX).

Fig. 8(c). Powders are available for Ti–Al–4V, Co-26Cr-6Mo among others to layer manufacture components as illustrated in Fig. 8(a).

Murr et al. (in press) have examined and compared the microstructure – mechanical property relationships for simple cylindrical, EBM builds shown in Fig. 6, utilizing the Ti–6Al–4V Grade 5 powder represented in Fig. 7. Fig. 9 shows SEM views of an EBM-built cylinder while Fig. 10 shows an SEM view from the top surface of the cylindrical part (TS in Fig. 10(a)) and an optical metallographic view (Fig. 10(b)) through a transverse section cut from the top of the cylinder, illustrating a uniform, acicular α phase microstructure (with β along the phase boundaries) similar to that for wrought Ti–6Al–4V in Fig. 1(a); including the β phase sizes. Fig. 11 shows an optical metallographic image composition depicting the transverse and longitudinal section microstructure for a conceptually built cylinder as in Fig. 9, illustrating the build layer interface regions (arrows in Fig. 9) spaced ∼100 μm. The corresponding (average) Vickers microindentation hardnesses (HV) and Rockwell C-scale hardnesses (HRC) are also indicated in Fig. 11. The

Vickers microindentation hardness (HV) values shown for the EBM cylindrical product in Fig. 11 might be compared with an average value of HV 510 for the precursor Ti–6Al–4V powder illustrated in Fig. 7 (Murr et al., in press). Fig. 12 shows TEM bright-field views of the α phase structure and dislocation substructures for a transverse section cut from a cylindrical build as illustrated in Fig. 11. The dislocation density in Fig. 12(b) is $\sim 5 \times 10^9$ cm^{-2}.
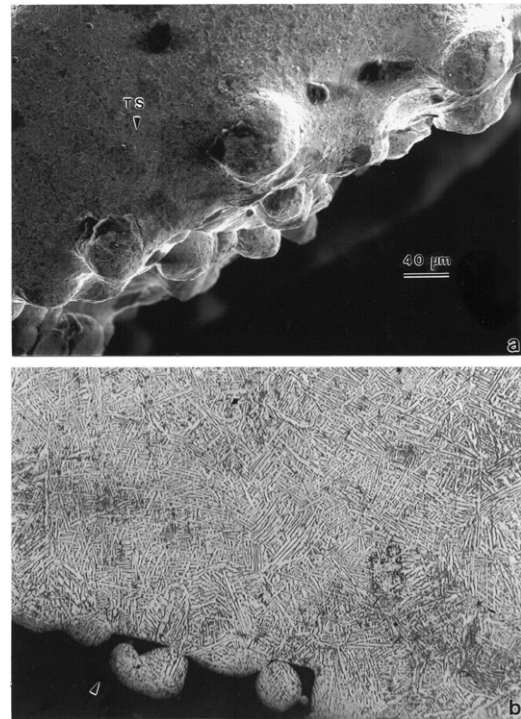
The mechanical properties for EBM-built cylindrical samples as illustrated in Figs. 9 and 11 have been measured (Murr et al., in press). The UTS was observed to range from 1.15 GPa to 1.20 GPa while the corresponding 0.2% engineering offset yield stress varied from 1.10 GPa to 1.15 GPa, respectively. Elongations were observed to range from 16% to 25%. The associated fracture surface features for the EBM cylindrical products compared very favorably with those observed for the wrought α phase Ti–6Al–4V product represented by Fig. 1(a) and as shown in Fig. 13. In examining the fracture surfaces of the EBM built specimens as in Fig. 13(a), there was no evidence of preferential failure at or within the layer interface or transition zones as illustrated in Fig. 11.
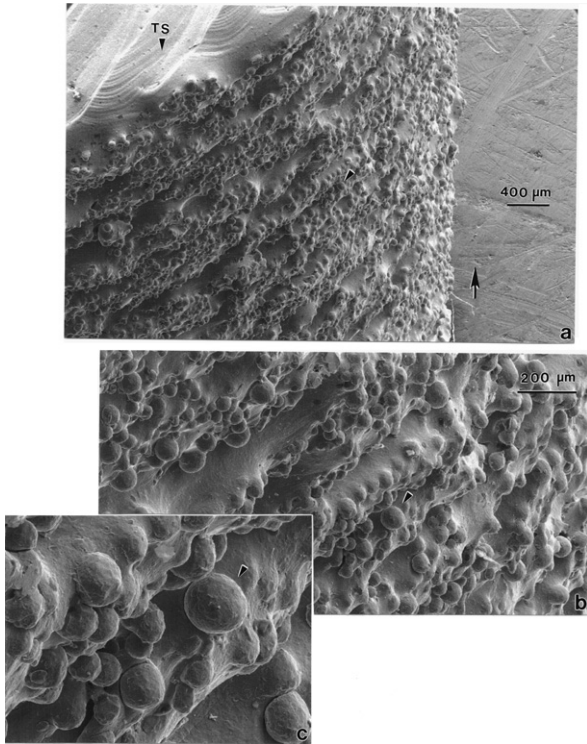
Fig. 9 – Field emission SEM views of an EBM cylindrical test sample built as illustrated schematically in Fig. 6. **(a) TS represents the top surface of the cylindrical build. (b) and (c) show magnified views of the cylindrical test build surface at reference arrows shown. The arrow to the right in (a) indicates the build direction. ((a) is from** Murr et al. (in press)**).**

Fig. 10 – Corresponding field emission SEM (a) and optical metallographic section view (b) for the cylindrical build sample in Fig. 9. **TS in (a) represents the top surface while the arrow in (b) designates the outer particle surface region. Magnification is shown in (a) for both (a) and (b). (From** Murr et al. (in press)**).**

4.   Direct digital manufacturing using selective laser melting (SLM): Microstructures and mechanical behavior of Ti–6Al–4V components

Fig. 14 illustrates a schematic view of the EOSINT M270 selective laser melting (SLM) or direct metal laser sintering (DMSL) system. This system builds layers approximately 30 μm thick from atomized powder represented in Fig. 15. Fig. 15(b) illustrates that this powder, in contrast to nominal EBM Ti–6Al–4V precursor powder shown in Fig. 7(b), has a skewed, smaller size distribution with an average particle size (diameter) of 21 μm. The smaller size powder for SLM facilitates laser beam melting in a nitrogen environment where the power (or energy) density in the 100–500 μm diameter beam is of the order of 190 W or as high as 10^2 kW/cm^2, comparable to the EBM system energy density in the building area. Beam and scan rate adjustments in SLM, like EBM manufacturing, can also allow for liquid-phase powder sintering as well. In contrast to EB scan rates, the laser beam in SLM scans nominally at 7×10^3 mm/s. As shown in Fig. 14 the machine comprises a process chamber with recoating system, an elevating system and platform heating module, an optical system with a ytterbium fiber laser operating at 1060–1100 nm, a process gas management system, and a process computer. The optical system creates and positions the laser beam (guided by an optical fiber,
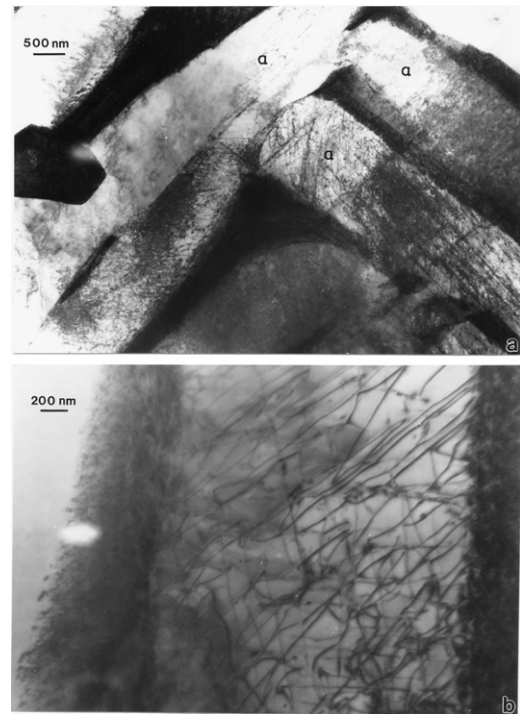
beam expander, scanner mirrors, and a focusing objective) to sinter or melt the precursor powder (Fig. 15(a)) which is applied to the building platform in a manner similar to the EBM process in Fig. 6. A platform heating module reduces temperature gradients between the building platform and the laser-sintered part to reduce internal stresses and ensure a good bonding of the first layers. It also removes moisture from the powder and helps to maintain the layer-built part at a constant temperature during any interruptions in the building process to ensure maximum process reliability.

Figs. 16 and 17 illustrate two product geometries built in the SLM system shown in Fig. 14 utilizing the powder shown in Fig. 15. Fig. 16 shows a predominantly α' martensite microstructure which, on average, has a Vickers microindentation hardness 24% greater than that for the EBM product represented in Fig. 11 (5.2 GPa versus 4.2 GPa) and a corresponding (average) Rockwell hardness (HRC) in Fig. 16 roughly 13% greater than that in Fig. 11. These hardness variances are similar on comparing the cylindrical build in Fig. 17 with Fig. 11 as well, and although the build directions are perpendicular. Note that Fig. 17 also illustrates the predominant α' martensite microstructure shown in Fig. 16. Some porosity is also evident in the build represented in Fig. 17. Fig. 18 shows the initial Ti–6Al–4V SLM process powder α microstructure and Vickers microindentation hardness measurement (average HV = 3.6 GPa) to be softer than the EBM process powder where the average microindentation hardness (HV) was 5.0 GPa (Murr et al., in press). Tensile
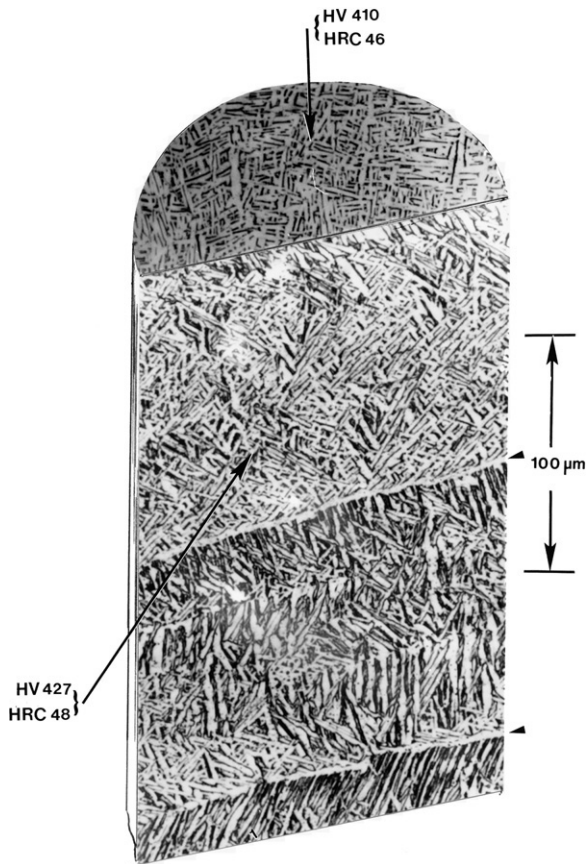
Fig. 11 – Exaggerated section views corresponding to optical metallographic images for the cylindrical Ti–6Al–4V build showing the average Vickers (HV) and Rockwell (HRC) hardness values. The microstructure is characterized by acicular α plates. The arrows to the right show the ~100 μm layer structures. The build direction is from bottom to top of figure.

Fig. 12 – Examples of TEM bright-field images of dislocation substructure in the α-plates of the cylindrical Ti–6Al–4V build represented in Fig. 11: **Transverse section views. (a) α phase grains and β (black) boundary/transition zones. (b) Magnified view showing dislocation substructure in α. (From Murr et al. (in press)).**

data measured for horizontal cylindrically built specimens (measuring 2 cm diameter and 12 cm in length originally), as represented conceptually in the optical metallographic image compositions in Fig. 17, also illustrated a UTS increase of 23% over the EBM vertically built cylindrical product represented in Fig. 11; and a corresponding drop in elongation by 78%. These features are shown for comparison in Fig. 19 which can also be compared with wrought and cast Ti–6Al–4V tensile data illustrated in Fig. 2. Fig. 20 illustrates typical views of the SLM cylindrical product fracture surface corresponding to tensile testing shown in Fig. 19. These fracture features can be compared with those common to the EBM produced cylindrical product and the wrought (α) Ti–6Al–4V product shown for comparison in Fig. 13. A marked decline in ductile dimple fracture features is observed for the SLM product fracture shown in Fig. 20 in contrast to the more ductile fracture features represented in the corresponding SEM images in Fig. 13. Fig. 20 shows small size, shallow dimples on quasi-cleavage fracture surfaces in contrast to large, ductile dimples for the EBM product in Fig. 13. This is consistent with the pronounced drop in elongation shown for comparison in Fig. 19.

Failure of biomedical implants is dominated by fatigue or fatigue-related failure such as fretting fatigue which are affected by various factors (mean stress, frequency or stress cycling, etc.). Wear or wear resistance can also be an issue (Niinomi, 2008). It is of course unclear at present whether SFF manufacture of biomedical implants, etc. can provide a significant improvement in wear or fatigue behavior.

Fig. 21 shows for comparison TEM bright-field images characteristic of the optical metallographic views of the α' martensitic microstructures shown in Figs. 16 and 17, respectively. While the martensitic plate spacings in Figs. 16 and 17 are consistent with those shown for the acicular α spacings in Fig. 11 (~2 μm), the TEM microstructure images in Fig. 21 show very fine, nano-grain α' with some intermixed α'' (fc-orthorhombic phase: $a = 0.30$ nm, $b = 0.49$ nm, $c = 0.46$ nm) (SAED pattern insert in Fig. 21(b)) having thicknesses and corresponding spacings between 0.1 μm and 0.3 μm; a factor of ten decrease from the acicular α-phase structure spacing in the EBM product (Figs. 11 and 12). This microstructural feature difference can account for the increase in hardness and tensile strength (UTS) noted above for the SLM built products, and implicit on comparing the tensile data illustrated in Fig. 19 for EBM and SLM built cylinders.

Barreda et al. (2001) have discussed differences in the α' content in electron beam welded (EBW) Ti–6Al–4V plates in contrast to plasma arc welded Ti–6Al–4V plates where
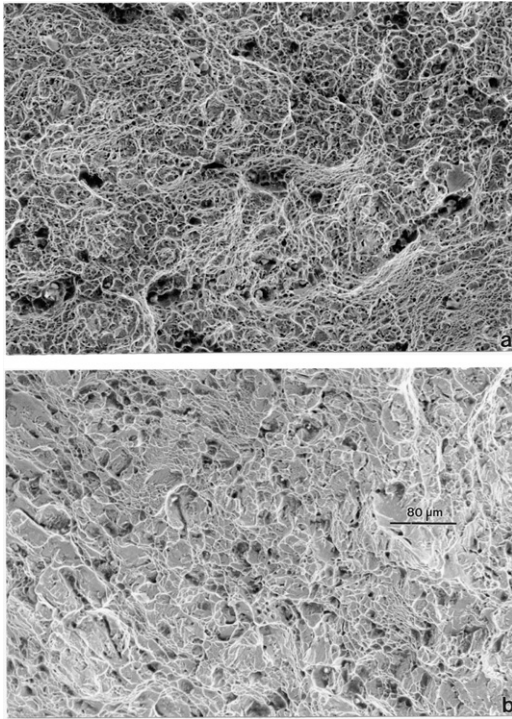
Fig. 13 – Comparison of fracture surface features for the EBM manufactured cylinder (Fig. 11) (a) and the wrought α-phase billet (Fig. 1(a)) (b). (a) corresponds to an elongation of 16% while (b) corresponds to an elongation of 12%. Magnification is the same as shown in (b).
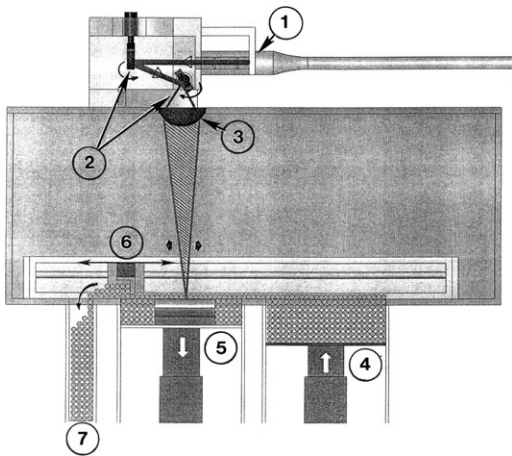
Fig. 14 – SLM system schematic showing key components: (1) Laser; (2) Double rotating mirror system; (3) Beam focus lens. The beam is scanned over the layer-building part (double arrows); (4) Powder feeder system; (5) Building platform; (6) Recoater (similar to powder rake in EBM system in Fig. 6); (7) Powder recovery/recycle.

the EBM material contained considerably more α' martensite. While these are characteristically different processes than layer manufacturing using SLM, these process differences provide some rationale for the significant, residual microstructural differences between the EBM products versus
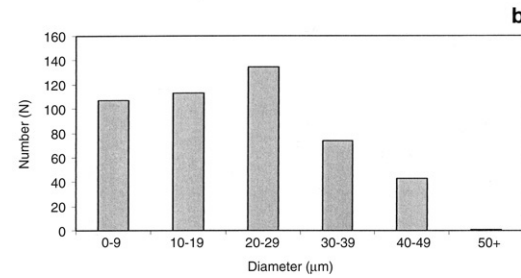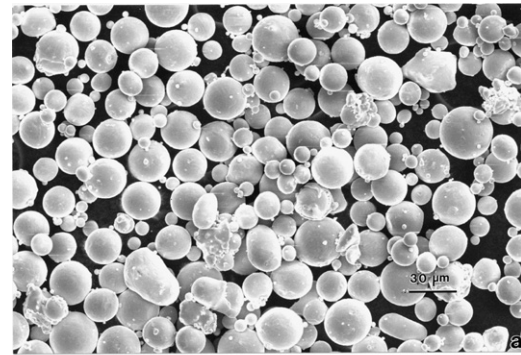
Fig. 15 – SLM system starting Ti–6Al–4V (Grade 5) powder features. (a) Field emission SEM image showing powder morphologies and sizes. (b) Histogram showing powder size distribution.

the SLM products: α-phase microstructure for the EBM product (Figs. 11 and 12) in contrast to the α'-phase microstructure of the SLM product (Figs. 16, 17 and 21). The EBM process involves more significant melt than the SLM process and process thermal issues are correspondingly different, including thermal gradients or associated, effective product quenching which is apparently responsible for the propensity of α' in the SLM product.

Deformation-induced α' is a common occurrence in Ti-alloys containing unstable β phase in their microstructures, and enhances fatigue strength (Iman and Gilmore, 1983), fracture toughness (Niinomi et al., 1990), fatigue crack propagation (Niinomi et al., 1993), and ductility (Niinomi, 1995), except where the martensite is process-induced prior to crack initiation or propagation (Akmoulin, 1994); as demonstrated in Fig. 19. The reduction of α phase microstructure dimensions by processes like TCP also correspondingly increases tensile (and fatigue) strength in $\alpha + \beta$ Ti–6Al–4V, as illustrated in Fig. 2.

5. Comparative advantages and disadvantages of EBM and SLM in contrast to wrought Ti–6Al–4V manufactured products

The standard production methods for generic mass-produced medical implants involves 5-axis or 6-axis CNC machining of bar stock. A typical knee implant component machined from bar stock produces as much as 80% metal waste chips. Lengthy machining times, material and equipment costs not only exacerbate generic component production, but in many instances generic components will not work well with patients having abnormal anatomy, requiring reconstruction of the patient joint to fit the implant. The custom design of
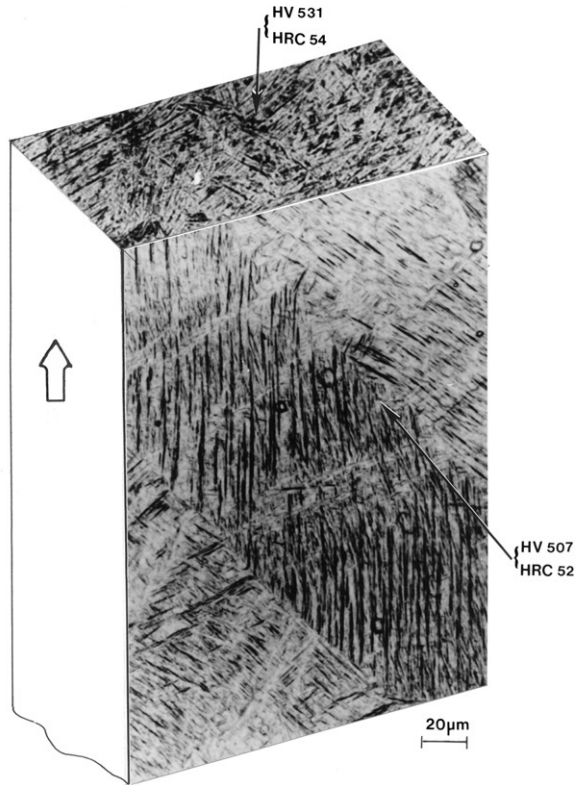
Fig. 16 – Exaggerated section views corresponding to optical metallographic images for a SLM rectangular build showing the average Vickers (HV) and Rockwell (HRC) hardness values (transverse (top) and longitudinal (face) sections). The microstructures are characterized by primarily martensite (α') plates. There are no apparent layer features. The large arrow at the left shows the build direction.
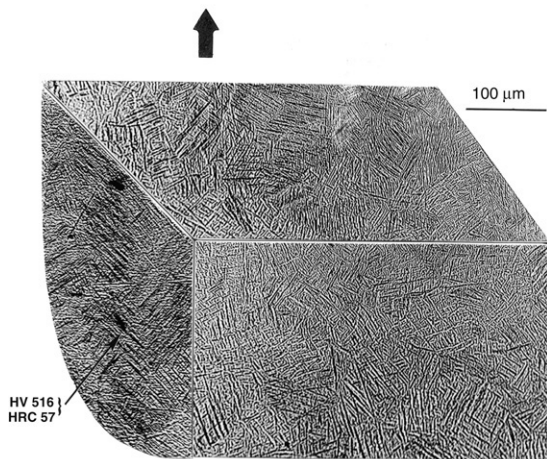

Fig. 17 – Exaggerated quarter section views corresponding to optical metallographic images for a horizontal cylindrical SLM build showing the average Vickers (HV) and Rockwell (HRC) hardness values. The microstructures show α' martensite with prior β boundaries. The large arrow (top) shows the build direction.
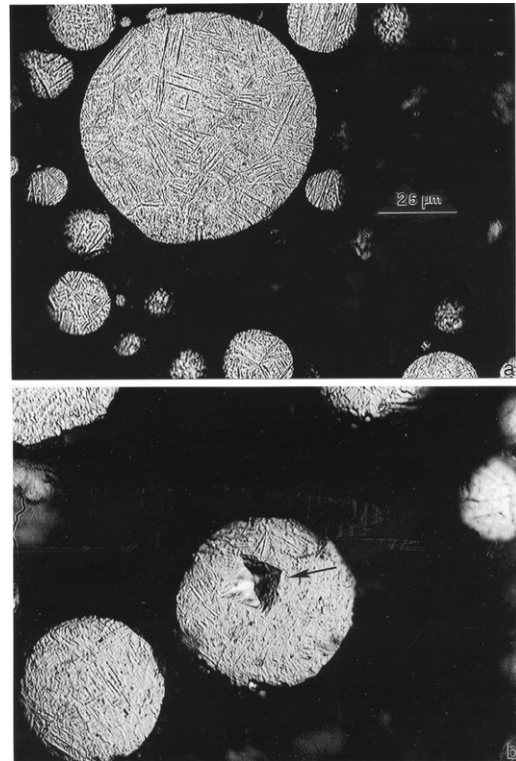
Fig. 18 – Optical metallographic views of SLM starting powder (Ti–6Al–4V) particle cross-sections. Magnification is the same as shown in (a).
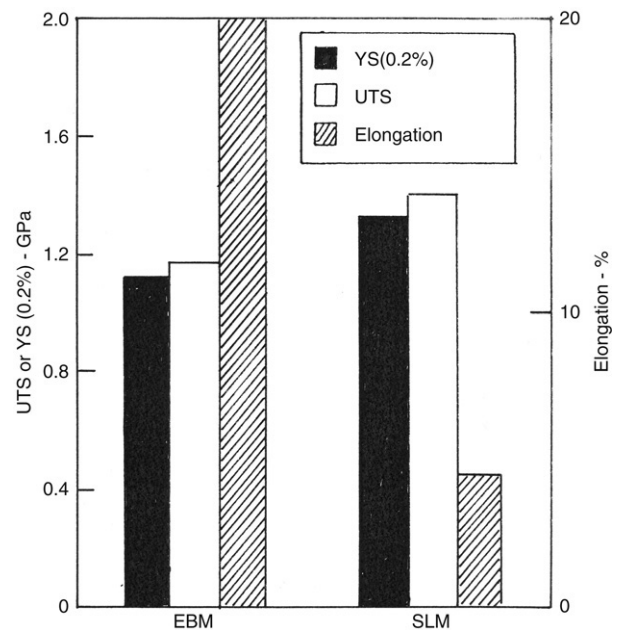

Fig. 19 – Ultimate tensile strength (UTS), 0.2% engineering offset yield stress (YS) and elongation (%) for EBM vertical cylinder build compared with SLM horizontal cylinder build.

implants circumvents these issues but can add considerable expense utilizing conventional manufacturing technologies.

Fig. 20 – Field emission SEM images showing fracture surface features for SLM manufactured (horizontal) cylinder corresponding to elongation of 4.4%.
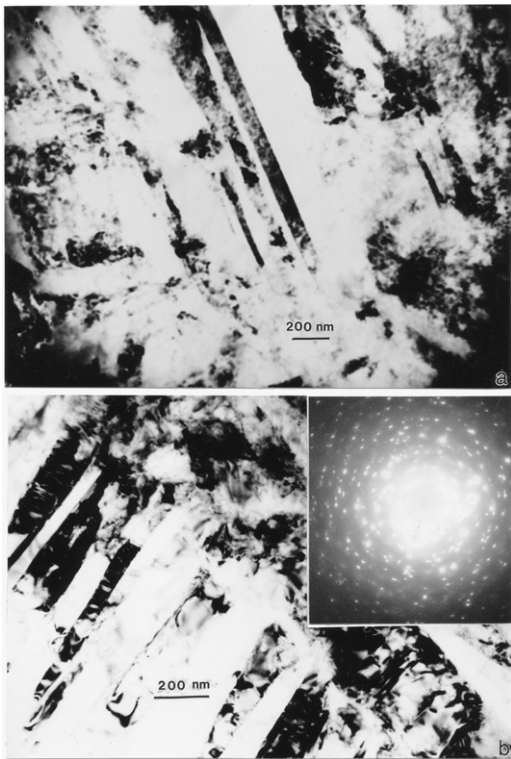
Fig. 21 – TEM (bright-field) image showing α' martensite nano-grain microstructure in the SLM vertical rectangular build (a) and horizontal cylindrical build (b) corresponding to Figs. 16 and 17, respectively. (b) shows some intermixing of α' and α'' phase (SAED pattern insert). (a) is directed into the build plane in Fig. 16 while (b) is in the plane perpendicular to the horizontal cylindrical build represented in Fig. 17.

Powder metallurgy offers a number of advantages in the production of a range of medical devices such as refined microstructures with isotropic properties and near-net-shape parts with high materials utilization (considerably reduced waste) implicit on comparing Fig. 8(a) and (b). Powder technologies include metal injection molding (MIM) and micro-MIM, and hot isostatic pressing (HIP). Of course EBM

and SLM technologies reviewed herein are also inclusive powder metallurgy processes.

Harrysson and Cormier (2005) have recently examined the EBM production of custom Ti knee implants using recommended process parameters which required 10 to 12 h to build a nested batch: a production rate of ∼1 to 1.5 h per implant per machine. For a machine producing 2 batches of implants/day for 5 days/week, one EBM machine (Fig. 6) could produce ∼4000 custom knee implants/yr. at a cost of roughly $150 to $200 each; far more cost and time effective than CNC machining of custom implants from Ti bar stock. Christensen (2007) has also recently discussed issues in qualifying EBM for the production of Ti–6Al–4V medical implants in the US. A significant feature of both EBM and SLM layer manufacture is significant waste material reduction since the unused powder can be recycled (Christensen, 2007). However, powder recycle is subject to some contamination or oxidation which may limit recycling to some extent. In addition, the initial powder material properties are of some importance and can be manipulated to some extent, although atomized powder microstructures tend to be similar (compare Figs. 7 and 15). However, note that on comparing Figs. 7 and 15 there is a notable difference in the average hardness: ranging from 3.6 to 5.0 GPa. There is of course the necessity for precision surface finishes on products such as knee implants as illustrated in Fig. 8, and this will add cost to the total manufacturing process.

Build microstructure and layer dimensions can be controlled to some extent by initial powder sizes and size distribution variations as shown for example in Figs. 7 an 15 as well as variations in process parameters: beam energy, scan rate, scan rate, scan pattern sequence, etc. Variations of these parameters in both the EBM and SLM systems can alter the sintering-to-melt regime, including variations in liquid-phase sintering to melt. These variations are somewhat implicit on comparing EBM products represented by Fig. 11 with SLM products represented by Figs. 16 and 17. The variations in process temperatures and associated thermal phenomena (including part cooling by heat conduction and associated quenching features) give rise to the microstructure and microstructural variations shown for the EBM products represented by Fig. 11 in contrast to those shown for the SLM products represented by Figs. 16 and 17. This points up the ability to selectively vary part microstructure and residual mechanical properties within narrow build dimensions (possibly 50 to 100 μm). Residual product tensile properties shown on comparing EBM and SLM in Fig. 19 with those for wrought and cast Ti–6Al–4V products in Fig. 2 demonstrate tensile strength variations in layer manufactured products ranging to 50% greater than wrought products with corresponding changes in elongation as ranging from ∼4.4% to 25%. Significantly higher residual harnesses in layer manufactured products may also provide significant advantages in wear applications as well.

As recently noted by Niinomi (2008), the Young's modulus as well as tensile strength (UTS), ductility (elongation) and other functionalities (collectively referred to as mechanical biocompatibilities) should be adjusted to levels suitable for structural biomaterials used in implants that replace hard tissue. Beta-type conventional Ti alloys especially exhibit

these biocompatibilities, but prospects for the development of specific functionalities through rapid prototyping (EMB and SLM) appear encouraging. Additionally, porous implants in particular can have bone-matching moduli which minimize or eliminate the "stress-shielding effects" of implants (Niinomi, 2008), and these porosity-related functionalities also appear to be a tractable feature of either EBM or SLM layer-manufactured, biomedical components. The Young's modulus can be conveniently controlled by simply varying the porosity ratio (Song et al., 1999). Oh et al. (2003) have shown a relationship between the Young's modulus and porosity for porous Ti samples made of Ti powder having different diameters in comparison with the Young's modulus of bulk Ti. Krishna et al. (2008) have recently described engineered porous metal implant manufacturing using laser-engineered net shaping (LENS). Consequently EBM and SLM can potentially build multiporous products as well as multi-microstructural products; e.g. those composed of α, β, $\alpha + \beta$, or α'. These multifunctional capabilities of layer manufacturing combined with the ability to build complex custom products from any 3D CAD design, with little finish machining, provide considerable advantages over conventional manufacturing.

Harrysson and Cormier (2005) have demonstrated porous network structures created by the EBM process which include a wide range of pore sizes and shapes resulting by variations in the intensity and duration of powder heating. This functionality affords a method for producing porous bone ingrowth surfaces on custom implants which is not possible by conventional manufacturing processes. The ability to fabricate complex scaffold products using either EBM or SLM is also a recognized advantage of layered manufacturing.

6.   Summary

Solid freeform fabrication (SFF) methodologies or rapid (prototype) manufacturing have been demonstrated to be extremely successful in fabricating complex shapes of custom-designed components from CT or other 3D CAD data utilizing polymer or ceramic powders to build these components layer-by-layer. In this review we have demonstrated the EBM and SLMS processes to be viable layer manufacturing technologies utilizing metal or alloy powders; specifically Ti–6Al–4V atomized powders which can be produced in a range of particle sizes and size distributions. Both the EBM and SLM processes can produce a wide range of characteristic crystallographic phases — α (hcp), β (bcc), α' (hcp martensite) and α'' (fc-orthorhombic) and phase microstructure which for conventional wrought and cast Ti–6Al–4V billets and bar stock require complex thermo-mechanical processing. EBM and SLM produced products representing precursors for biomedical implants have demonstrated the ability to build simple geometries having a microstructure which gives rise to a mechanical behavior similar to and superior to wrought or cast Ti–6Al–4V products. Tensile strengths have ranged from 1 to 1.45 GPa, a 50% increase over wrought products; with corresponding elongations ranging from 25% to 4.4%. Corresponding residual hardnesses ranged from HRC 37 to 54.

Future research addressing the use of various starting powders or variations of process parameters to produce specific microstructures and microstructural variations during the build process will make EBM and SLM truly multi-functional materials manufacturing processes which are not achievable using conventional powder metallurgy techniques or wrought and cast precursors. While the fabrication of custom implants in particular will cost more than generic, mass-produced implants utilizing CNC toolpath manufacturing, the ability to recycle waste powder and selectivity tailor desirable properties and performance should compensate for cost differences and eventually eliminate significant cost variances.

REFERENCES

Akmoulin, I.A., et al., 1994. Dynamic fracture toughness of Ti–Al–4V alloy with various stabilities of β phase. Metall. Trans. A 25A, 1655–1666.

Akahori, T., et al., 2000. Effects of thermochemical treatment on properties of cast Ti-6Al-7Nb alloy for dental applications. J. Japan Inst. Met. 64, 895–902.

Barreda, J.L., et al., 2001. Electron beam welded high thickness Ti–6Al–4V plates using filler metal of similar and different composition to the base plate. Vacuum. 62 (2–3), 143–150.

Christensen, A., 2007. Qualifying EBM for production of Ti6Al-4V medial implants in the US. EBM User Group Meeting. Simi Valley, CA (November 15, 2007).

Christensen, A., Lippincott, A., Kircher, R., 2007. Qualification of electron beam melted (EBM) Ti–6Al–4V-ELI for orthopaedic implant applications. Medical Modeling LLC – Technical Report.

Chuna, C.K., Leong, K.F., Lim, C.S., 2003. Rapid Prototyping: Principles and Applications, 2nd ed. World Scientific, Singapore.

Cormier, D., Harrysson, O., West, H., 2004. Characterization of H13 steel produced via electron beam melting. Rapid Prototyping J. 10 (1), 35–41.

Destefani, J., 1990. Introduction to Titanium and Titanium Alloys, tenth ed. In: ASM Metals Handbook, vol. 2. pp. 586–591.

Ding, R., Guo, Z.X., Wilson, A., 2002. Microstructure evolution of a Ti–6Al–4V alloy during thermomechanical processing. Mater. Sci. Engng. A 327, 233–245.

Eufinger, H., Saylor, B., 2001. Computer-assisted prefabrication of individual craniofacial implants. AORH J. 74 (5), 648–654.

Eylon, D., Froes, F.H., 1990. Titanium P/M Products, tenth ed. In: ASM Handbook, vol. 2. pp. 647–660.

Eylon, D., Newman, J.R., Thorne, J.K., 1990. Titanium and Titanium Alloy Castings, tenth ed.. In: ASM Handbook, vol. 2. pp. 634–646.

Froes, F.H., et al., 2004. The Technologies of titanium powder metallurgy. JOM November 46–48.

Gibson, I. (Ed.), 2005. Advanced Manufacturing Technology for Medical Applications. J. Wiley & sons Ltd., London.

Harrysson, O.L.A., Cormier, D.R., 2005. Direct fabrication of custom orthopaedic implants using electron beam melting technology. In: Gibson, I. (Ed.), Advanced Manufacturing Technology for Medical Applications: Reverse Engineering, Software Conversion and Rapid Prototyping. John Wiley & Sons, Ltd., London, pp. 191–206 (Chapter 9).

Hiemenz, J., 2007. Electron beam melting. Adv. Mater. Processes 165, 45–46.

Iman, M.A., Gilmore, C.M., 1983. Fatigue and microstructural properties of quenched Ti–6Al–4V. Metall. Trans. A 14A, 233–240.

Krishna, V., Xue, W., Bose, S., Bandyopadhyay, A., 2008. engineered porous metals for implants. JOM May 45–48.

Lampman, S., 1990. Wrought Titanium and Titanium Alloys, tenth ed. In: ASM Handbook, vol. 2. pp. 592–633.

Leutjering, G., Williams, J.C., 2003. Titanium. Springer, New York.

Long, M., Rack, H.J., 1998. Titanium alloys in total joint replacement – a materials science perspective. Biomaterials 19 (18), 1621–1639.

Murr, L.E., 1991. Electron and Ion Microscopy and Microanalysis: Principles and Applications, 2nd ed. Marcel Dekker, Inc., New York.

Murr, L.E., et al. 2008. Microstructures and mechanical properties of electron beam – rapid manufactured Ti–6Al–4V biomedical prototypes compared to wrought Ti–6Al–4V. Mater. Characterization (in press).

Niinomi, M., et al., 1995. Mechanical properties and fracture characteristics of Ti–6Al–4V and Ti-5Al-2.5 Fe with refined microstructure using hydrogen. Metall. Mater. Trans. A 26A, 1141–1151.

Niinomi, M., 1998. Mechanical properties of biomedical titanium alloys. Mater. Sci. Engng. A243, 231–236.

Niinomi, M., 2001. Recent metallic materials for biomedical applications. Met. Mater. Trans. A 32A, 477–486.

Niinomi, M., 2007. Recent research and development in metallic materials for biomedical, dental and healthcare products. Mater. Sci. Forum. 539–543, 193–200.

Niinomi, M., 2008. Mechanical biocompatibilities of titanium alloys for biomedical applications. J. Mech. Behavior Biomed. Mater. 1, 30–42.

Niinomi, M., et al., 1990. The effect of deformation-induced transformation on the fracture toughness of commercial titanium alloys. Metall. Trans. A 21A, 1733–1744.

Niinomi, M., et al., 1993. Fatigue crack propagation in Ti–6Al–4V alloys. In: Fores, F.H., Caplan, I. (Eds.), Titanium, vol. 92. TMS, pp. 1835–1842.

Oh, I.H., et al., 2003. Mechanical properties of porous titanium compacts prepared by powder sintering. Scripta Mater. 49, 1197–1202.

Sakaguchi, N., et al., 2004. Deformation behaviors of Ti-Nb-Ta-Zr system alloys for biomedical applications. Mater. Trans. 45, 1113–1119.

Song, Y., et al., 1999. Theoretical study of the effects of alloying elements on the strength and modulus of β-type bio-titanium alloys. Mater. Sci. Engng. A260, 269–274.

Vandenbroucke, B., Kruth, J.-P., 2007. Selective laser melting of biocompatible metals for rapid manufacturing of medical parts. Rapid Prototyping J. 13, 196–203.

Williams, J.C., Leutjering, G., 1980. The effect of slip length and slip character on the properties of titanium alloys. Titanium 80, Science and Technology 1, 671–681.

Williams, J.C., Chesnutt, J.C., Thompson, A.W., 1987. The effects of microstructure on ductility and fracture toughness of alpha + beta titanium alloys. Microstructure, Fracture Toughness and Fatigue Crack Growth Rate in Titanium Alloys. Denver, Colorado USA, February, pp. 255–271.

Yaszemski, M.J., et al. (Eds.), 2004. Biomaterials in Orthopedics. Marcel Dekker, Inc., New York.